



# Numerical analysis and modeling of jacketed rod penetration

Brett R. Sorensen<sup>a,\*</sup>, Kent D. Kimsey<sup>a</sup>, Jonas A. Zukas<sup>b</sup> and Konrad Frank<sup>a</sup>

<sup>a</sup> U.S. Army Research Laboratory, Aberdeen Proving Ground, MD 21005-5066, U.S.A.

<sup>b</sup> Computational Mechanics Associates, P.O. Box 11314, Baltimore, MD 21239-0314, U.S.A.

Received 31 January 1998; in revised form 8 August 1998

---

## Summary

A computational study to assess terminal ballistic performance issues of adding a steel sheath, or jacket, to a depleted uranium (DU) penetrator has been performed. The CTH hydrocode was used to model DU penetrators with steel sheaths of various thicknesses against semi-infinite rolled homogeneous armor (RHA), finite RHA, and oblique plate targets. Guided by the initial results, additional semi-infinite RHA simulations were performed to support the development of a generalized penetration model for jacketed rods. The model computes RHA penetration as a function of impact velocity and normalized jacket thickness (thickness over diameter) and compares very favorably with experimental DU and steel data. The model indicates that “bulk” density (areal density) can considerably underestimate jacketed rod penetration. In addition, some insight into the penetrator and target flow shape factors ( $k_p$  and  $k_t$ ) is obtained. © 1998 Elsevier Science Ltd. All rights reserved.

**Keywords:** Numerical analysis; Modeling; Jacketed rod penetration; Terminal ballistic performance

---

## Notation

$a$	penetration parameter
$b$	penetration parameter
$D$	penetrator diameter
$H$	target “resistance”
$k_p$	penetrator shape factor
$k_t$	target shape factor
$L$	penetrator length
$P$	penetration

---

\* Corresponding author.

$T$	jacket thickness
$v$	impact velocity
$Y$	penetrator “strength”
$\alpha$	penetration parameter
$\rho$	density

## 1. Introduction

The sheathed, or jacketed, penetrator concept is certainly not novel. Small-caliber ammunition has been using jackets for many years. In the large-caliber, kinetic energy (KE) tank ammunition arena, several developmental and fielded projectiles have utilized jacketed penetrators in the past due primarily to the poor mechanical properties of the high-density alloys available at that time. By placing a jacket on the penetrator, problems associated with launchability and target interaction were alleviated. As the mechanical properties of high-density materials improved, the need for a jacket diminished and terminal ballistic evaluation showed that a jacket degraded performance. Thus, the use of jacketed penetrators in KE tank ammunition ceased.

Recent trends in KE armor-piercing ammunition are toward higher aspect ratio penetrators and increased velocity. Cartridge-based systems studies have shown that increased length and aspect ratio tend to maximize penetration performance [1–3]. Since limits exist on length (due to system constraints), increased aspect ratio remains a primary avenue to improve KE ammunition performance. However, as the aspect ratio increases beyond a certain point, significant technological hurdles appear in one or more phases of the ballistic cycle, placing doubt on the effectiveness of monolithic KE penetrator solutions against future armor systems.

To extend the life of KE weapons, studies examining alternate lethal mechanisms have been initiated. Within these efforts, two main thrusts exist: increasing penetrator efficiency or capacity, and minimizing or eliminating certain armor effects. Various concepts proposed and studied include, but are not limited to, segmented penetrators, rod-tube penetrators, sliding (extending) penetrators, and noncircular cross-section penetrators. These solutions tend to be complex, and many require supporting technologies that make fielding a long-term proposition. A simpler, short-term concept under consideration is to sheath, or jacket, the penetrator [4–8]. The goal here is to launch the maximum length penetrator, at elevated velocities, without encountering the aeroballistic problems associated with extreme aspect ratio. The key is to design the penetrator so that the sheath influences interior and exterior ballistics in the most favorable manner, without detracting from terminal ballistic performance.

With the advent of supercomputers and sophisticated analysis packages, sufficient tools exist today to study the phenomenology of a jacketed penetrator at each phase of the ballistic cycle. This paper discusses a study conducted to examine the penetration mechanics of jacketed penetrators. The CTH finite volume code was used to simulate the penetration event. Penetrators with a length-to-diameter ratio ( $L/D$ ) of 10 were employed in this study to make the CPU time of each simulation reasonable. It was felt that any differences in performance due to increased  $L/D$  would manifest as a simple offset and will not distort the basic behavior. The goal was to observe how a steel jacket on a depleted uranium (DU) penetrator affects penetration, and then determine how to minimize any adverse effects, and if possible, develop a generalized penetration model.

## 2. Simulations and modeling

### 2.1. Numerical aspects of jacketed rod penetration

A number of calculations were undertaken to examine the terminal ballistic effects of steel jacketed, DU penetrators striking semi-infinite and finite thickness rolled homogeneous armor (RHA) targets. The first phase of calculations considered the five sets of initial conditions presented in Table 1. For each case, the thickness of the jacket was varied between the limiting cases of monolithic DU and steel penetrators, keeping the indicated parameters constant.

All calculations were performed with CTH [9], a second-order finite volume code designed to minimize the dispersion present in Euler codes. The Mie–Grüneisen equation-of-state option was used to compute the hydrodynamic component of the stress tensor. Deviatoric stresses were computed from an incremental elastic-perfectly-plastic model using split-Hopkinson bar data reported by Nicholas [10]. In the version of CTH used in these studies, fracture can be modeled based on pressure or principal stress. The pressure fracture criterion can be valuable in the presence of high-pressure gradients that occur during hypervelocity impact. In addition, tensile pressure cutoff criteria have been used successfully to model spallation in metal plates [11]. However, for ordnance velocity impacts where peak pressures are much lower and decay to the order of the material strength within one or two wave reverberations in the characteristic dimension, the use of a pressure criterion means that failure will not occur unless it occurs on the first passage of the reflected pressure pulse in the characteristic dimension. Using this option is equivalent to performing a calculation without accounting for failure. More realistic results can be obtained with strain-based criteria [12–14]. However, such a criterion was not available in CTH at the time these calculations were undertaken. Therefore, failure was based on principal stress exceeding material strength by a factor of 2.5. Comparisons for a few cases were made with calculation using a pressure-basis failure criterion. Little difference was observed between the two.

The mesh used a regular cell size of  $0.115 \times 0.115$  cm/cell, resulting in 20 cells across the penetrator diameter with at least two cells across the jacket. The penetrator core/jacket interface was placed on a computational grid line to prevent mixed cells and minimize diffusion. Standard CTH Johnson–Cook [15] parameters were implemented and are listed in Table 2.

Table 1  
Simulation matrix showing penetrator and target configurations

Case	Target	Parameters held constant				Variable parameters $f\{T/D\}$
		Diameter	Velocity	Energy	Mass	
1	Semi-infinite RHA	✓		✓		Velocity, mass
2	Semi-infinite RHA	✓				Energy, mass
3	Semi-infinite RHA		✓	✓		Diameter
4	150 mm RHA	✓	✓		✓	Energy, mass
5	250 mm RHA		✓	✓		Diameter
6 <sup>a</sup>	25.4 mm RHA @ 60°	✓	✓			Energy, mass

<sup>a</sup> Only monolithic DU and one specific jacketed penetrator geometry were modeled.

Table 2  
Johnson–Cook constitutive parameters

	Material	$A$ (MPa)	$B$ (MPa)	$n$	$C$	$m$
DU core	DU-0.75 Ti	1079	1120	0.25	0.007	1.00
Steel jacket	S-7 tool steel	1539	477	0.18	0.012	1.00
RHA target	4340 steel	792	510	0.26	0.014	1.03

Each set of calculations for the various initial conditions began with a baseline calculation of a  $L/D$  10, DU rod ( $230 \times 23$  mm). This was followed by calculations where the sheath thickness was taken to be  $D/10$ ,  $D/5$ , and  $D/2.5$ , where  $D$  represents the diameter of the rod. For some conditions, a steel rod was also considered. In terms of the sheath thickness ( $T$ ) to projectile diameter ( $D$ ) ratio, the simulations spanned  $T/D$  ratios of 0.0 (DU rod), 0.1, 0.2, 0.4, and 0.5 (steel rod).

Since length is held constant in this study, penetrator diameter must increase as jacket thickness increases for the cases where penetrator mass is constant, resulting in  $L/D$ s of 10, 8.9, 7.6, and 6.6 for  $T/D$  ratios of 0.0, 0.1, 0.2, and 0.4, respectively. This introduces a difficulty in analyzing some of the data. Penetration per unit rod length,  $P/L$ , is known to be dependent on  $L/D$ . Therefore, the difference in  $L/D$  for the constant mass cases must be accounted for when discussing the results.

One last issue to discuss prior to presenting the results is the assumption on the initial condition of the interface between the penetrator core and jacket. To ensure adequate shear stress distribution between the core and jacket at launch, a traction mechanism (e.g., threads, shrink fit) will be required. This traction mechanism would prevent the occurrence of an axial velocity gradient across the interface during the interior and terminal ballistic phases. However, a radial velocity difference would remain possible as the jacket can radially separate (expand) from the core. (A localized axial velocity difference is now possible in this region.) Modeling this type of interface is possible in structural finite elements, but not in Eulerian finite volume codes. Here, the interface must be unconstrained, or constrained in both the axial and radial directions. As the latter case was felt to be more appropriate, a constrained interface was adopted for this study. While this interface condition effectively locks the interface, the jacket can still separate from the core, but the resulting shear stresses would be much larger than could be supported for any manufacturing process. Other interface conditions will be examined in the future.

#### 2.1.1. Semi-infinite target penetration

Results for the semi-infinite target calculations are shown in Table 3 and more succinctly in Fig. 1. Depending on which parameters are held constant, the results indicate that a thin sheath ( $T/D \approx 0.1$ ) either does not detract from the rod's penetrability or enhances it slightly. For increasing sheath thickness, there is a corresponding degradation of penetration depth for all cases considered. While an optimum sheath thickness has not been determined in this study, it is clearly in the neighborhood of  $D/10$ .

The constant energy curve (Case 1) in Fig. 1 differs in shape from the constant velocity and constant mass curves (Cases 2 and 3) and also shows an increase in performance. To provide a different view of the data and to also validate the results, Fig. 2 plots normalized penetration

Table 3  
Semi-infinite RHA penetration results

Case number	$T/D$	Rod diameter (mm)	Sheath thickness (mm)	Rod mass (kg)	Striking velocity (m/s)	Impact energy (MJ)	$P/L$	Residual length (mm)
1 (Constant energy)	0.0	23.0	—	1.777	1700	2.568	1.14	10.8
	0.1	23.0	2.3	1.406	1911	2.568	1.24	8.0
	0.2	23.0	4.6	1.117	2144	2.568	1.26	8.8
	0.4	23.0	9.2	0.787	2555	2.568	1.03	13.5
	0.5	23.0	—	0.745	2626	2.568	0.88	7.8
2 (Constant velocity)	0.0	23.0	—	1.777	1700	2.568	1.14	10.8
	0.1	23.0	2.3	1.406	1700	2.032	1.09	13.5
	0.2	23.0	4.6	1.117	1700	1.614	0.92	29.3
	0.4	23.0	9.2	0.787	1700	1.137	0.59	38.8
	0.5	23.0	—	0.745	1700	1.137	0.59	38.8
3 (Constant mass)	0.0	23.0	—	1.777	1700	2.568	1.14	10.8
	0.1	25.8	2.6	1.777	1700	2.568	1.13	17.2
	0.2	30.3	5.8	1.777	1700	2.568	0.98	35.7
	0.4	34.8	13.8	1.777	1700	2.568	0.65	48.1
	0.5	34.8	—	1.777	1700	2.568	0.65	48.1

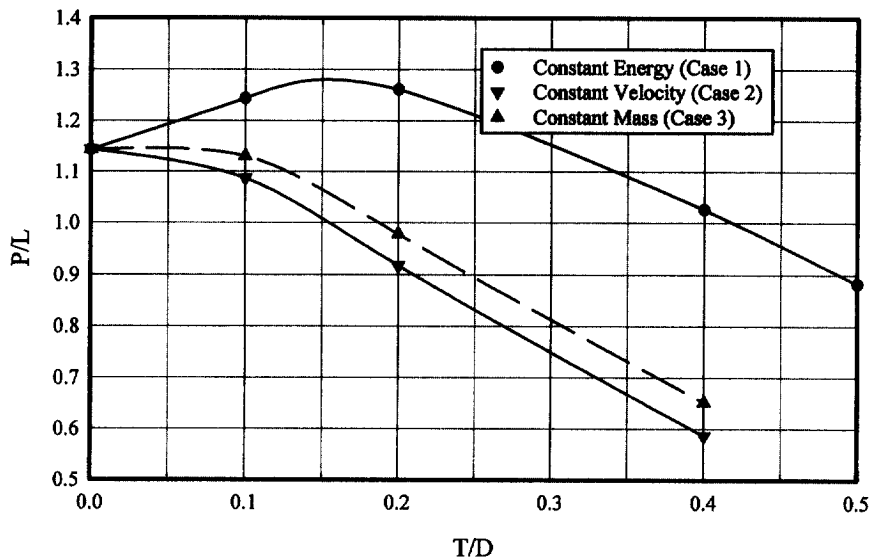


Fig. 1. Semi-infinite RHA penetration results:  $P/L$  versus  $T/D$ .

against striking velocity for the constant geometry cases (Cases 1 and 2) and nominally one-quarter scale,  $L/D$  10 DU and steel penetrators [16, 17]. Empirical fits to the experimental data have also been included. The constant mass curve (Case 3) has been omitted because the effects of aspect ratio could not be adequately accounted for.

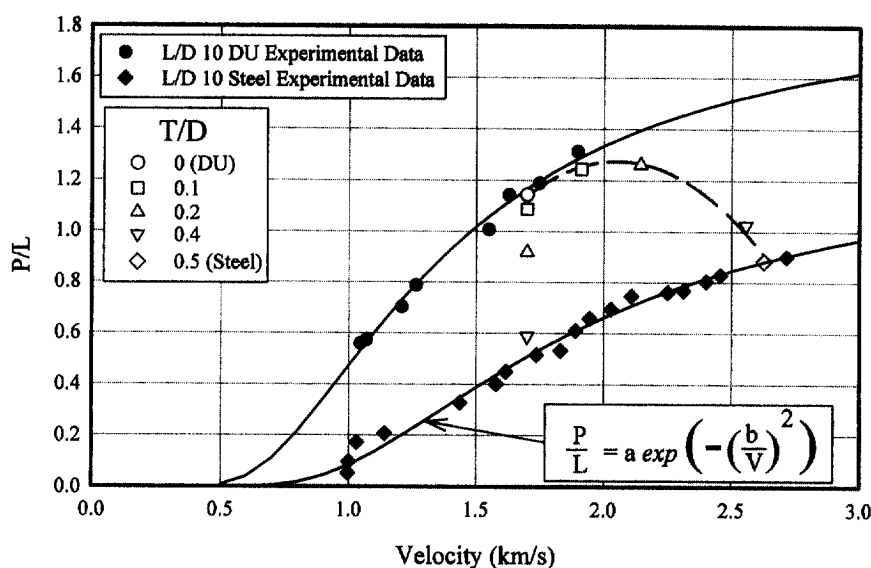


Fig. 2. Comparison of the constant diameter penetrator simulation results to one-quarter scale DU and steel experimental results.

Figure 2 shows that the simulations of the DU and steel penetrators agree quite well with the experimental results and also illustrates the effects of the competing mechanisms of increasing velocity and decreasing penetrator density for the constant energy case (Case 1). For the  $T/D = 0.1$  sheathed penetrator, the combination of decreasing density and increasing velocity produces a result not significantly different from a solid DU rod at the same velocity. However, for  $T/D = 0.2$  and beyond, decreasing density has started to dominate as normalized penetration is rapidly diverging from the DU penetration curve and approaching the steel penetration curve. Thus, the competing mechanisms of increasing velocity and decreasing penetrator density provides the nonmonotonic (parabolic) shape seen in the constant energy curve in Fig. 1. Figure 2 also shows that sheathed penetrator performance never exceeds solid DU penetrator performance even though Fig. 1 indicated the possibility.

Figure 3 shows the constant energy penetration curve (from Fig. 1) and the theoretical hydrodynamic limit as a function of  $T/D$ . The hydrodynamic limit<sup>1</sup> is specified by the square root of the ratio of the penetrator and target densities, where bulk density is assumed for the sheathed penetrators. It is interesting to see that in the range of  $T/D$ s between 0.15 and 0.4, performance exceeds the computed hydrodynamic limit. A possible explanation for this unexpected rise above the computed hydrodynamic limit follows. Using bulk density to compute hydrodynamic limit assumes a homogenized material. In reality, a high-density core is surrounded by a lower density

<sup>1</sup> The hydrodynamic limit is a theoretical limit that is obtained only for very high velocities (where the inertial terms are much larger than any material strength effects) and for very high  $L/D$  penetrators so that steady-state effects dominate the transient contributions at the beginning and end of the penetration process.

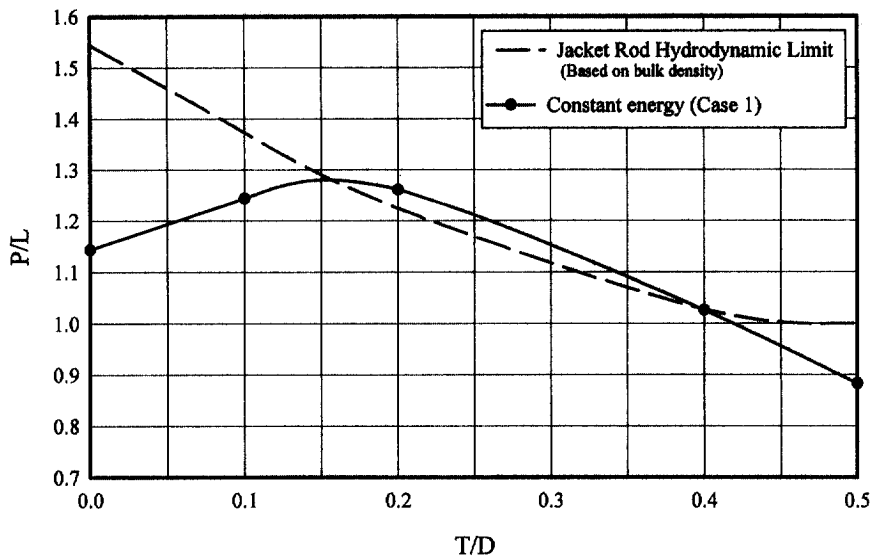


Fig. 3. Comparison of normalized jacketed rod penetration and the hydrodynamic limit (based on bulk density).

material. This material arrangement is apparently more efficient than the smeared density assumption gives credit for; so performance is increased beyond what the hydrodynamic limit, based on bulk density, would predict. This is supported by Ekbohm's *et al.*'s [4] proposal that a high-density, high-compressive-strength core be inserted into a thick, high-density jacket to advantageously modify target flow behavior, thereby increasing penetration.

In addition to bulk penetrator density, striking velocity appears to effect penetration characteristics as  $T/D$  varies. This is seen in Fig. 4 where the constant velocity and constant energy curves in Fig. 1 have been normalized by DU performance. Here, the penetration of each simulation was normalized by the penetration that a solid DU rod would have at the same velocity. If sheathed penetrator performance was insensitive to velocity, the constant energy and constant velocity curves should be very similar using this normalization scheme. This is not the case since increasing velocity seems to increase the performance of the sheathed rods. One argument is that higher velocities create a larger diameter crater, creating more room for the sheath and erosion products, decreasing the burden of the sheath. Regardless of the reason, the process appears to be quite complex and sophisticated models will be required for further analyses.

#### 2.1.2. Finite thickness target penetration at normal incidence

Table 4 indicates that the 150 mm RHA target is clearly overmatched by all projectile configurations considered. Again the thinnest of the sheath thicknesses considered ( $T/D = 0.1$ ) provides the best performance with regard to residual mass and residual KE. Performance then appears to degrade as sheath thickness is increased.

The 250 mm RHA target provides more of a challenge for the projectiles. The baseline DU rod perforates the target with a residual velocity of 1,050 m/s and a residual length of 20 mm, while the projectile with the smallest sheath thickness perforates with a residual velocity of 930 m/s but

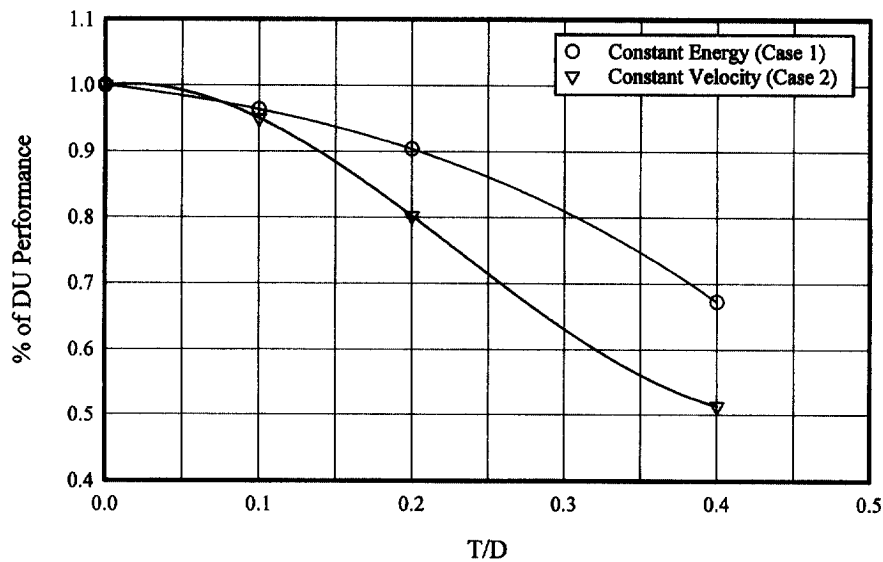


Fig. 4. Semi-infinite RHA penetration results normalized by expected monolithic DU penetration at equal velocity.

a considerably larger residual length of 30 mm. The residual energy of the sheathed projectile is again higher than that of the DU rod. Thus, there is an interesting trade-off here in terms of lethality. A thin sheath produces a residual penetrator moving at a slower velocity compared to that of a DU rod but possessing considerably more mass.

Even though penetrator aspect ratio varies for the 250 mm target, the fact that the  $T/D$  0.2 and 0.4 ( $L/D$  7.9 and 6.6) penetrators did not perforate the target permits further analysis. By examining residual energy, only the  $T/D$  0.0 and 0.1 results apply, and since the performance difference between  $L/D$  10 and 8.9 penetrators is relatively small, the difference in aspect ratio can be ignored.

The residual energy data from Table 4 is plotted in Fig. 5 for both the 150 and 250 mm targets. Since penetrator mass was not constant for the 150 mm target, residual energy has been normalized by impact energy. This figure illustrates that a  $T/D = 0.1$  sheath will maintain a larger percentage of the rod's initial energy after perforation.

### 2.1.3. Finite thickness target perforation at oblique incidence

Figures 6(a) and (b) depict the state of a DU and sheathed ( $T/D = 0.1$ ) penetrator,  $L/D = 10$ , 350  $\mu$ s after impact of a 25.4 mm RHA target at 68° obliquity with a striking velocity of 1700 m/s. Residual lengths and velocities are approximately the same, but the sheath serves to inhibit bending to a considerable extent. Thus, a thin sheath could prove useful in enhancing the effectiveness of projectiles with intermediate  $L/D$  ratios, i.e.,  $5 < L/D < 15$ .

The calculation was repeated with rods having an  $L/D$  of 30. For this length, there was no discernible difference between sheathed and bare rods at 350  $\mu$ s after impact. One theory for the different response is that the increased length reduced the number of wave reflections occurring before 350  $\mu$ s, effectively decreasing the amount of time for deflections to occur. If the calculation were permitted to run longer, the response between the short and long penetrators may have been



Table 4  
Finite RHA penetration results

$T/D$	Rod diameter (mm)	Sheath thickness (mm)	Rod mass (kg)	Striking velocity (m/s)	Impact energy (MJ)	Residual velocity (m/s)	Residual length (mm)	Residual energy (MJ)
<i>Case 4: 150 mm RHA — constant velocity and diameter</i>								
0.0	23.0	0	1.777	1700	2.568	1530	92	0.832
0.1	23.0	2.3	1.406	1700	2.032	1500	97	0.667
0.2	23.0	4.6	1.117	1700	1.614	1370	89	0.406
0.4	23.0	9.2	0.787	1700	1.137	600	52	0.032
<i>Case 5: 250 mm RHA — constant velocity, mass, and energy</i>								
0.0	23.0	0	1.777	1700	2.568	1050	20	0.085
0.1	25.9	2.6	1.777	1700	2.568	930	30	0.100
0.2	29.0	5.8	1.777	1700	2.568	0.0 <sup>a</sup>	30	0
0.4	34.6	13.8	1.777	1700	2.568	0.0 <sup>b</sup>	75	0

<sup>a</sup> Limit velocity.

<sup>b</sup> Partial penetration.

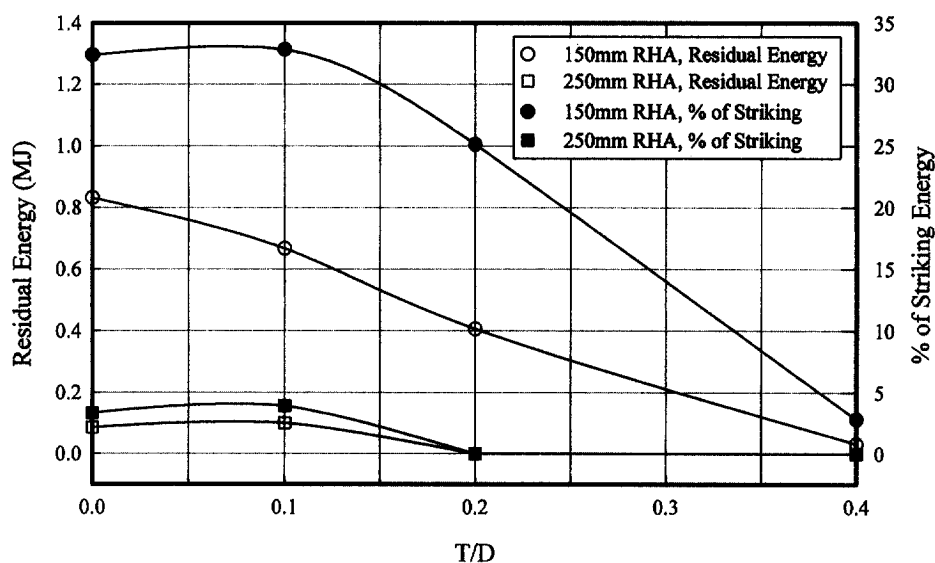


Fig. 5. Residual penetrator kinetic energy versus  $T/D$  for the finite RHA perforations.

more similar. However, in the real world of high-aspect-ratio penetrators and compact armors, the result indicating no difference in shape between the monolithic DU and the jacketed penetrators could be expected for this target.

A conclusion can be made from these results that, from the standpoint of terminal ballistics, a thin sheath may marginally improve penetrator performance. At worst, it will not significantly

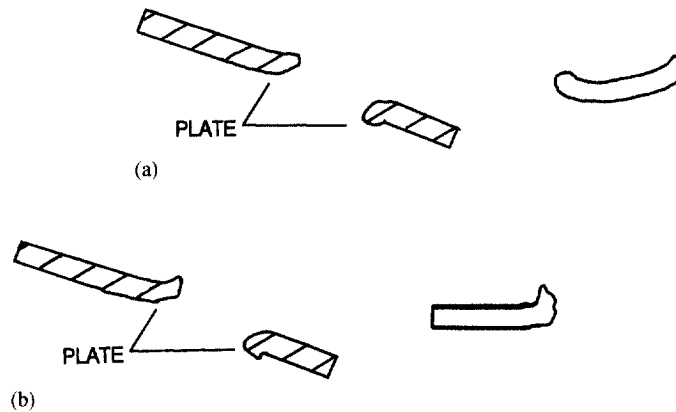


Fig. 6. DU and  $T/D = 0.1$  jacketed rods 350  $\mu$ s after striking a 25.4 mm RHA plate at 60°.

degrade it. Sheaths have been used traditionally on projectiles with weak cores to ensure integrity during launch and flight. Hence, the payoff for sheathed penetrators may lie in areas other than penetration.

### 3. Penetration modeling

Since resources were not available to conduct an experimental terminal ballistic program to validate the simulation results, the results from Section 2.1.1 were expanded and used to develop a semiempirical penetration model for steel sheathed DU penetrators. The successful completion of this effort will not only provide a useful model, but also increase the confidence in the simulation results until experiments can be performed. The additional simulations were performed at striking velocities of 1.2 and 3.0 km/s using the same assumptions discussed in Section 2.1. Penetrator geometry was kept constant except for varying jacket thickness. All of the simulation results to be used for model development are listed in Table 5.

A generic penetration model for sheathed penetrators has been developed using Frank's extension of the Lanz–Odermatt penetration function as related to the Alekseevskii–Tate penetration parameters [18]. Frank's formulation of the Lanz–Odermatt function is a two-parameter, exponential fit relating striking velocity to normalized, semi-infinite penetration [see Eqn (1)]. Values for  $a$  and  $b$  can be determined from a set of experimental data provided that the range of penetrator aspect ratios and scale is appropriate and a sufficient range in velocity exists. The veracity of this form has already been demonstrated in Fig. 2 by fitting the DU and steel experimental data. Figure 7 illustrates the result of fitting the simulation results (open symbols and dashed lines) to Eqn (1) as well as the experimental data (solid symbols and lines). The resultant values for  $a$  and  $b$  are listed in Table 6.

$$\frac{P}{L} = a \exp\left(-\frac{b^2}{v^2}\right). \quad (1)$$

Table 5  
Semi-infinite penetration results

$T/D$	Rod mass (kg)	Striking velocity (m/s)	Impact energy (MJ)	$P/L$	Striking velocity (m/s)	Impact energy (MJ)	$P/L$
0.0	1.777	1700	2.568	1.14	1200	1.279	0.68
0.1	1.406	1911	2.568	1.24	1200	1.012	0.59
0.2	1.117	2144	2.568	1.26	1200	0.804	0.43
0.4	0.787	2555	2.568	1.03	1200	0.567	0.21
0.5	0.745	2626	2.568	0.88	1200	0.536	0.18
0.0	1.777	1700	2.568	1.14	3000	7.997	1.62
0.1	1.406	1700	2.032	1.09	3000	6.327	1.59
0.2	1.117	1700	1.614	0.92	3000	5.027	1.54
0.4	0.787	1700	1.137	0.59	3000	3.541	1.20

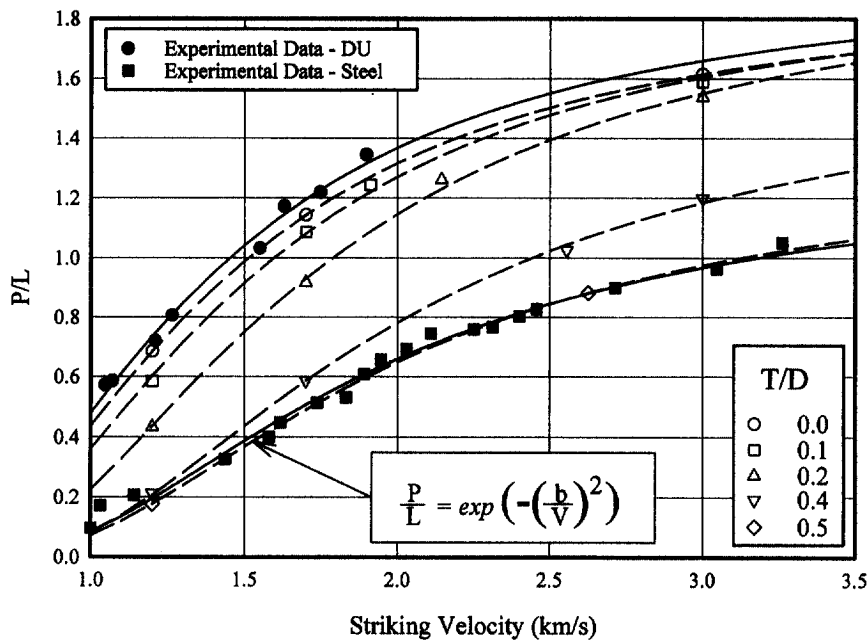


Fig. 7.  $P/L$  versus velocity for the simulation and experimental data. Curve fits are provided for both the simulation and experimental data sets.

The form of Eqn (1) fits both the experimental and simulation data well. For the DU experimental data, a very good median curve is provided for the limited and slightly scattered data. However, in the case of the steel experimental data, an exceptional fit is provided for a range of velocities from 1.0–3.5 km/s. For the simulation data, each curve represents the data quite well, the curves do not cross and an interesting trend becomes obvious. At high velocities, the performance of the thinner jacketed penetrators approaches that of a DU penetrator and the performance of

Table 6

Results of a two-parameter, exponential fit to the experimental and simulation penetration data

	DU	Steel	$T/D = 0.0$	$T/D = 0.1$	$T/D = 0.2$	$T/D = 0.4$	$T/D = 0.5$
$a$	1.940	1.313	1.902	1.934	1.976	1.652	1.349
$b$	1.182	1.659	1.213	1.296	1.475	1.730	1.710

thick jacketed penetrators diverges from that of a steel penetrator, further evidence that performance may not be driven entirely by bulk density. Finally, comparing the curve fits of the monolithic rods (i.e., simulation versus experimental for  $T/D$ s of 0.0 and 0.5) shows that the steel experimental and simulation curves are very similar, which is not the case for the DU where the simulation curve appears to be offset from the experimental curve. Although the DU simulations appear to compare well with the DU experiments, the simulation results were always on the lower boundary of the experimental results, resulting in the consistent shift of the two curves. Previous work by Zook and Magness (unpublished data) also demonstrated this trend of the DU simulations slightly under predicting penetration when compared to this same experimental data.

With what appears to be a pattern in the simulation results, the task at hand is to find it and develop a model. After a detailed examination of Table 6, the parameters appear of little value directly because additional physical parameters governing the penetrator–target interaction are embedded in the two parameters. However, some insight can be gained by comparing the results of Eqn (1) with results similar to that of Alekseevskii–Tate model, which describes the interaction process with four basic parameters: the penetrator and target flow shape factors  $k_p$  and  $k_t$ , and, the penetrator and target material “strength” (flow stress) values  $Y$  and  $H$  (see Eqns (2a) and (2b)). In Odermatt’s formulation,  $\alpha$  represents an expression for aspect ratio, which approaches one as aspect ratio exceeds 20. (In this paper,  $\alpha$  represents a free variable, embodying aspect ratio and other late time effects.) Thus, for long rod penetrators ( $L/D > 20$ ), if  $k_p$  and  $k_t$  are assumed equal (typically  $k_p$  and  $k_t$  are assumed to be 0.5), term  $a$  may simplify to the expression for the hydrodynamic limit. The term  $(H - Y)/(k_p \rho_p)$  is the square of the cutoff velocity, relating the  $b$  term to penetrator/target interaction as well.

$$a = \alpha \sqrt{\frac{k_p \rho_p}{k_t \rho_t}}, \quad (2a)$$

$$b^2 = \left(1 + \sqrt{\frac{k_p \rho_p}{k_t \rho_t}}\right) \left(\frac{H - Y}{k_p \rho_p}\right). \quad (2b)$$

Even though the parameters in the empirical model have been related to analytic functions, the model must be adapted to the case at hand before it can be useful. An inventory of the variables in Eqns (2a) and (2b), referenced against available information, results in five unknowns,  $\rho_p$ ,  $k_p$ ,  $k_t$ ,  $\alpha$  and the term  $(H - Y)$ . This assumes that target density is known and that the terms  $a$  and  $b$  can be determined (Table 6). By using a homogenized (bulk) penetrator density,  $k_p$  and  $k_t$  can then be computed from the simulation results once  $\alpha$  and  $(H - Y)$  are specified. Using these values for  $k_p$  and  $k_t$ , functions (curve fits) with respect to  $T/D$  can be obtained, which then permit  $a$  and  $b$  to be computed for any  $T/D$ .

If the previous assumption that  $k_p$  and  $k_t$  should be equal and near 0.5 is continued for monolithic penetrators striking RHA, then Eqns (2a) and (2b) and the data from Table 6 can be used to determine  $\alpha$  and  $(H - Y)$  for both DU and steel. Inserting the  $a$  and  $b$  terms resulting from the exponential fits of the small scale,  $L/D$  10, experimental data into Eqn (2a) yields values for  $\alpha$  of 1.26 and 1.31 for DU and steel penetrators, respectively. Solving Eqn (2b) yields values for  $(H - Y)$  of 5.1 and 5.3 GPa, respectively. Since  $(H - Y)$  for DU rods impacting steel targets has been reported to be in the range of 4–5 GPa, and for steel versus steel,  $(H - Y)$  can be up to 1 GPa less [19], the value of 5.1 GPa for DU rods is certainly reasonable, but the value of 5.3 GPa for steel rods appears to be inconsistent. This discrepancy could be caused by the assumption that  $k_p = k_t = 0.5$  for both DU and steel rods. If  $\alpha$  is assumed constant at 1.26 and  $(H - Y)$  to be 4.1 GPa for steel rods, then  $k_p = 0.39$  and  $k_t = 0.36$  for the steel data, making  $k_p$  and  $k_t$  nearly equal, but approximately 25% smaller than for DU. Since little is known about  $k_p$  and  $k_t$ , using a linear function in  $(T/D)$  for  $(H - Y)$  is a good starting point, i.e.,

$$(H - Y) \left\{ \frac{T}{D} \right\} = 5.1 - 2 \left( \frac{T}{D} \right) \quad (3)$$

where the brackets on the left-hand side of Eqn (3) denotes that  $(H - Y)$  is a function of  $T/D$ .

Once functions for  $\alpha$  and  $(H - Y)\{T/D\}$  are assumed, sufficient information exists to determine expressions for  $k_p$  and  $k_t$  as a function of  $T/D$  for the simulation data. Two options exist for determining the expressions for  $k_p$  and  $k_t$  as functions of  $T/D$ : use the simulation data for the jacketed rods ( $T/D$ s = 0.1, 0.2, and 0.4) and a second-order curve fit; or, use all of the simulation data ( $T/D$ s = 0.0, 0.1, 0.2, 0.4, and 0.5) and the appropriate curve fit. The first option groups like simulations of the composite rods to generate a model that extrapolates to the monolithic rods and the experimental data, while the second method uses a larger data set. Instead of discussing the merits of each option, both will be investigated.

Starting with the assumptions that  $\alpha$  is constant at 1.256 and that  $(H - Y)\{T/D\} = 5.1 - 2(T/D)$ ,  $k_p$  and  $k_t$  can be computed from the  $a$  and  $b$  terms in Table 6. The results are plotted in Fig. 8 where the simulation data are seen as open symbols and the experimental data as the filled symbols. The solid curves represent second-order least square fits to the  $k_p$  and  $k_t$  data for the jacketed rod simulation data only ( $T/D = 0.1, 0.2$ , and  $0.4$ ). The broken lines are second- and third-order fits to all five of the simulation  $k_p$  and  $k_t$  data points. Several observations can be made from Fig. 8. First, the agreement between the experimental and simulation results for  $k_p$  and  $k_t$  at  $T/D$ s of 0.0 and 0.5 is quite good. Second, the solid curves fit the data very poorly. And third, while the second-order fit to all of the simulation data provides adequate results (a maximum error of 10%), the third-order fits are clearly better. Since the curves obtained from the jacketed rod data only (solid curves) are clearly inadequate, this method of obtaining functions for  $k_p$  and  $k_t$  will be dropped from further consideration.

Using the functions just obtained for  $k_p$  and  $k_t$  (fits to all five data points), Eqn (1) can now be solved to compute  $P/L$  as a function of striking velocity and  $T/D$ , the results of which are plotted in Fig. 9. Here again, the solid symbols and lines represent the experimental data and curve fits whereas the open symbols represent simulation results and the broken lines the resulting penetration model from Eqns (1) and (2). The first, and most important observation, is that the model appears to have captured the major elements in predicting penetration. Although there are some discrepancies, the model matches both the simulation and experimental data quite well.

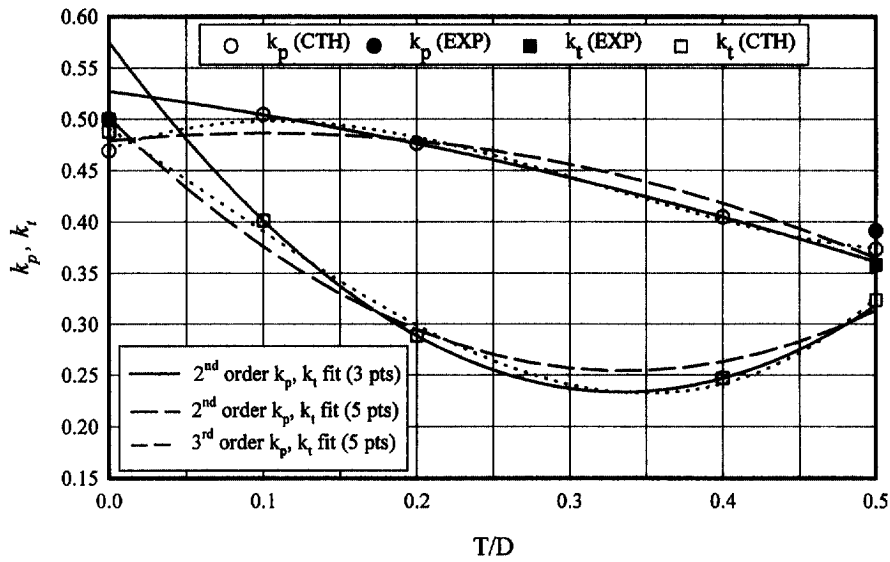


Fig. 8. Resulting  $k_p$  and  $k_t$  values using  $a$  and  $b$  parameters from Table 6, Eqns (2a) and (2b), and values of 1.256 for  $\alpha$  and  $(H - Y)\{T/D\} = 5.1 - 2(T/D)$ .

Furthermore, while the two plots appear quite similar, there is an important difference to note. Comparing the exponential curve fits to the simulation data in Fig. 7 with the curves resulting from the penetration model in Fig. 9, it is seen that the  $T/D$  0.0 curve intersects the  $T/D$  0.1 curves in Fig. 9 instead of converging at high velocity as seen in Fig. 7. However, the velocity at which the intersection occurs increases and the amount of divergence decreases as the fits to the  $k_p$  and  $k_t$  data improve.

To thoroughly examine linear functions of  $(H - Y)\{T/D\}$ , the function  $(H - Y)\{T/D\} = 5.1 - x(T/D)$  was studied where  $x$  was varied to return values for  $(H - Y)\{0.5\}$  between 1 and 7 GPa. For each  $(H - Y)\{T/D\}$ , the associated standard and average errors between the data and the penetration model were computed and examined for both the second and third order fits to  $k_p$  and  $k_t$ . These results showed that the errors were minimized for values of  $(H - Y)\{0.5\}$  in the range of 3.5 to 4.0 GPa, agreeing with previous statements about  $(H - Y)\{T/D\}$  and supporting the use of  $(H - Y)\{T/D\} = 5.1 - 2(T/D)$ . Furthermore, these errors (Table 7) indicate that the model is matching the data extremely well.

In an attempt to provide additional improvement to the penetration model, the constraint on  $(H - Y)\{T/D\}$  being linear was relaxed. A family of second-order curves was examined where two conditions were met:  $\alpha$  and  $(H - Y)\{0\}$  were set to keep  $k_p = k_t = 0.5$  for  $T/D = 0$  and  $(H - Y)\{0.5\} = (H - Y)\{0\} - 1$ . The resulting  $k_p$  and  $k_t$  data that produced the best penetration results are displayed in Fig. 10. Comparing Figs 8 and 10,  $k_p$  and  $k_t$  are the same for  $T/D = 0.0$  and  $0.5$  but different elsewhere, in fact, the  $k_p$  curve has inverted. Examination of the errors in Table 7 indicates that the penetration results for a second order  $(H - Y)\{T/D\}$  are no more accurate than the linear function for  $(H - Y)\{T/D\}$ , however, plots of the penetration results show that the constant  $T/D$  lines do not cross at high velocity, but converge as seen in Fig. 7, providing the best

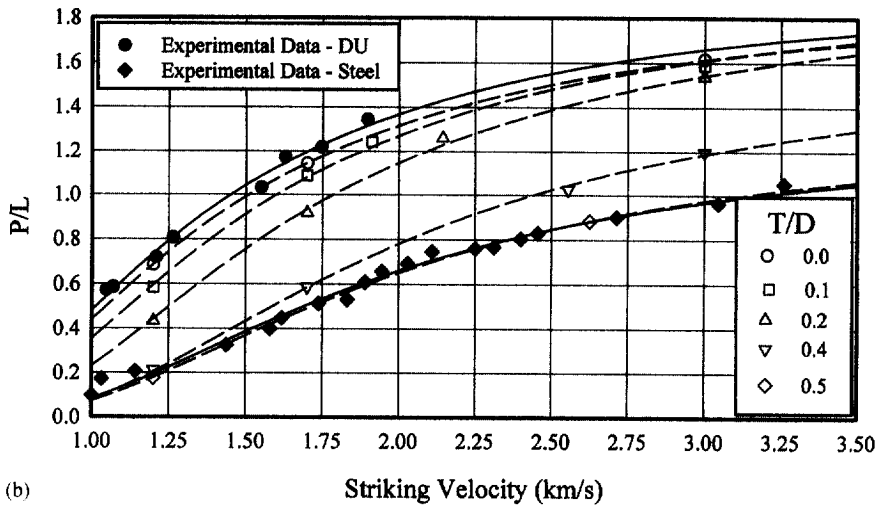
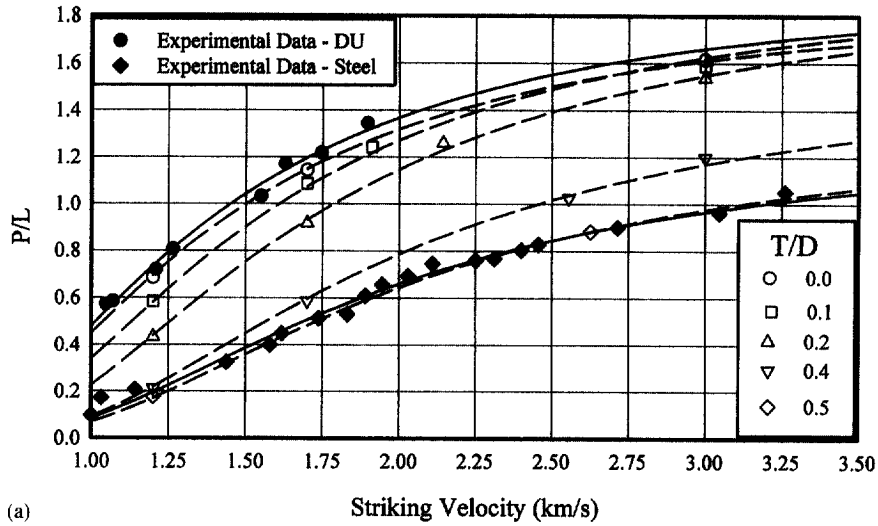


Fig. 9. Penetration model results using the better sets of  $k_p$  and  $k_t$  functions displayed in Fig. 8. (a) Second order fit to all of the simulation results. (b) Third order fit to all of the simulation results.

combination of results so far. However, to obtain this result,  $(H - Y)\{T/D\}$  uses values as low as 3.9 GPa (Fig. 11). If values of 5.1 and 4.1 GPa for  $(H - Y)\{T/D\}$  at  $T/D$ s of 0.0 and 0.5 are appropriate, an argument could be made that for  $T/D$ s between 0.0 and 0.5,  $(H - Y)\{T/D\}$  should be bounded by its values at  $T/D$ s of 0.0 and 0.5. However, given the assumptions made already and how little is known about the actual values of  $k_p$  and  $k_t$ ,  $(H - Y)\{T/D\}$  was permitted to have small excursions beyond the limits set by  $T/D$ s of 0.0 and 0.5.

Returning to the issue of appropriate assumptions, first consider that bulk density is used in the analysis and that previous discussion indicated that this assumption may not accurately predict

Table 7

Resulting standard and average errors between the data and the penetration model for various input options

Type of ( $H - Y$ ){ $T/D$ } function	Order of $k_p, k_t$ fit	CTH <sup>a</sup>		DU <sup>b</sup>		Steel <sup>b</sup>	
		Standard error (%)	Average error (%)	Standard error (%)	Average error (%)	Standard error (%)	Average error (%)
Linear	2	0.021	1.8	4.4	2.3	1.8	2.3
Linear	3	0.014	1.3	4.9	1.2	1.1	1.4
2nd order	2	0.012	1.9	4.2	2.2	2.2	2.2
2nd order	3	0.027	1.4	4.8	1.4	1.4	1.4

<sup>a</sup> Error between the model and the CTH simulations used to generate the model.

<sup>b</sup> Error between the model and the experimental data.

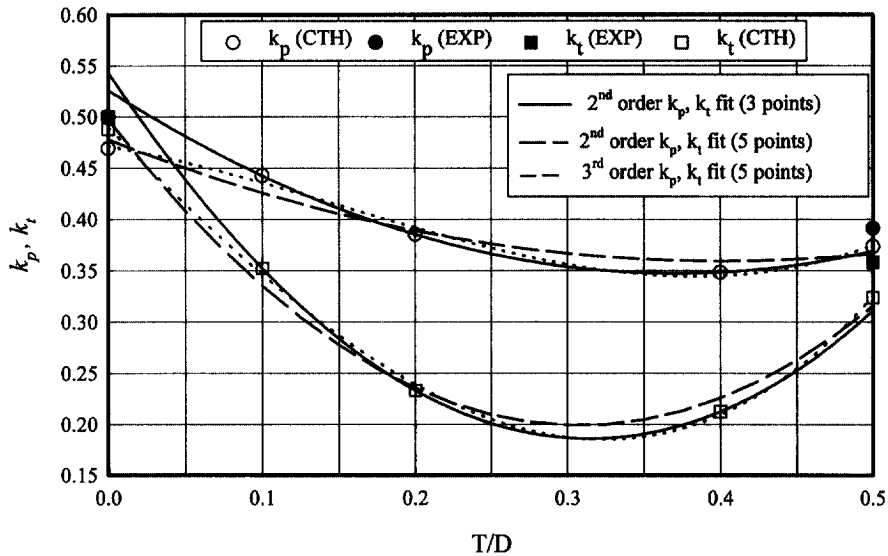


Fig. 10. Resulting  $k_p$  and  $k_t$  parameters using a second-order function for  $(H - Y)\{T/D\}$ .

penetration performance. Using the simulation results from Fig. 7, the velocity at which  $P/L$  equals the hydrodynamic limit can be determined for both  $T/D$ s of 0.0 and 0.5. (For this discussion, hydrodynamic limit is defined by the square root of the density ratio.) Using these velocities, 2653 m/s for  $T/D = 0.0$  and 3117 m/s for  $T/D = 0.5$ , to construct a line, one could argue that the velocity for which  $P/L$  equaled the hydrodynamic limit for any other  $T/D$  would lie on the line (see path 1 in Fig. 12). By making this assumption and also assuming that target density is constant, an effective penetrator density can be computed for any  $T/D$ . These results are found in Table 8 and Fig. 13, clearly illustrating that the bulk density assumption is not sound. In addition to the



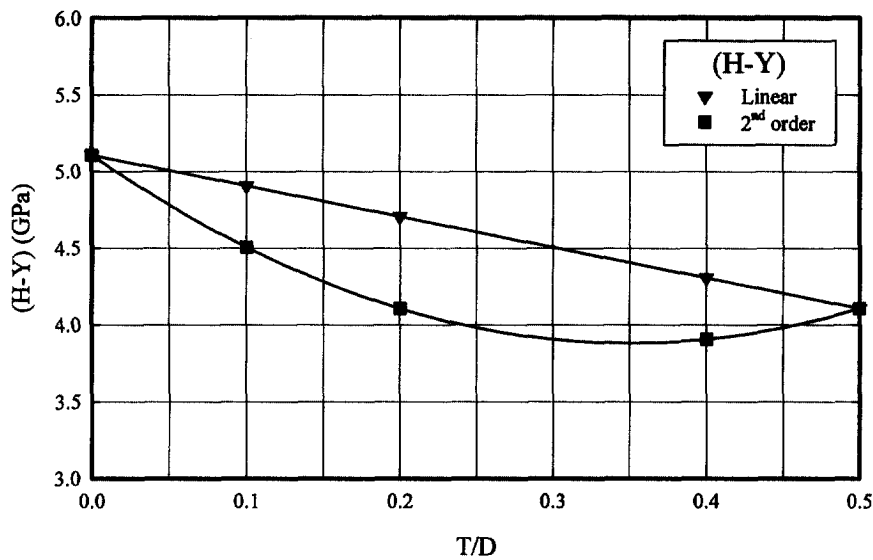


Fig. 11. Linear and second-order forms of  $(H - Y)\{T/D\}$  producing the “best” penetration model results.

Table 8  
Bulk and effective density comparison

$T/D$	0.0	0.1	0.2	0.4	0.5
Bulk density ( $\text{kg/m}^3$ )	18,600	14,712	11,688	8232	7800
Hydrodynamic limit (bulk density assumption)	1.544	1.373	1.224	1.027	1.000
Hydrodynamic limit (from linear interpolation)	1.543	1.493	1.435	1.159	1.000
Velocity (m/s)	2653	2692	2775	3022	3117
Effective density ( $\text{kg/m}^3$ )	18,600	18,322	17,266	11,054	7800

straight line (path one in Fig. 12), three nonlinear cases are also presented to further demonstrate that due to material orientation, bulk density does not reflect performance accurately and to show that the effective density is relatively insensitive to the path, or hydrodynamic velocity profile, chosen. Furthermore, the shape of the effective density curves are consistent with arguments made in Section 2.1.1.

At this point, an argument could be supported that the effective densities listed in Table 8 should be used for penetrator density in Eqn (2b) instead of bulk density. However, making this substitution had little effect on the resulting penetration model, and since bulk density is a known quantity, its use remains more attractive (within this model) than an expression for effective density. Nevertheless, valuable insight could be gained by examining the subtleties of changes like using

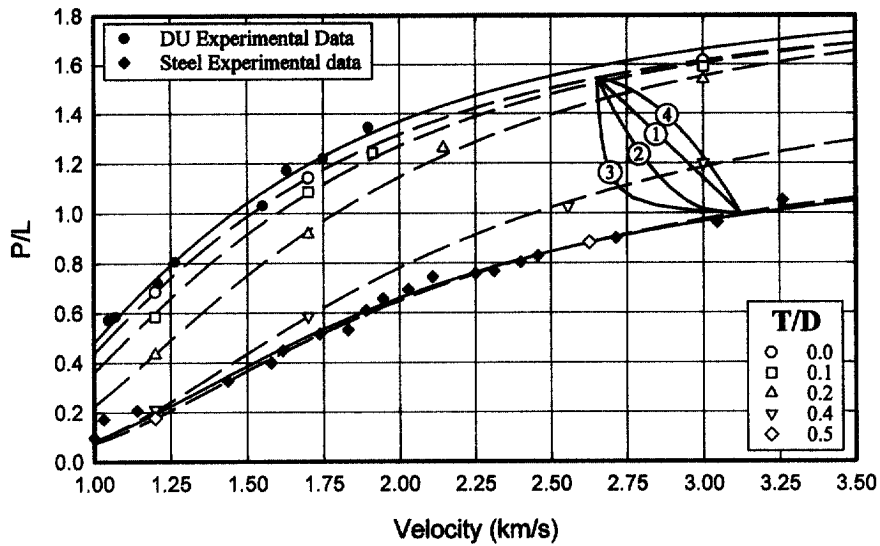


Fig. 12. Possible  $P/L$  versus velocity profiles to follow to achieve the hydrodynamic limit as  $T/D$  varies from 0.0 to 0.5.

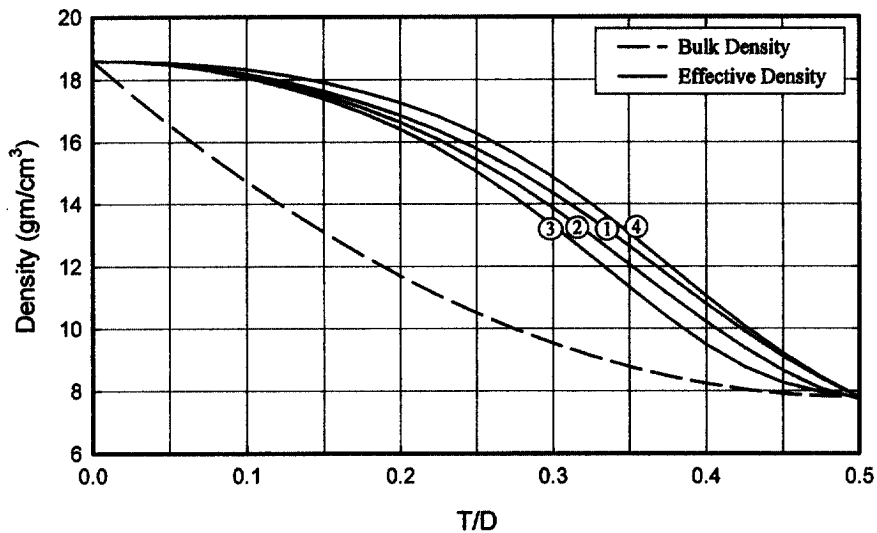


Fig. 13. Theoretical densities obtained from the hydrodynamic limit as a function of  $T/D$  for various  $P/L$  versus velocity profiles.

effective density in place of bulk density; because in this case, the resulting  $k_p$  curve is nearly the same as the  $k_t$  curve as  $T/D$  varies from 0 to 0.5 and this relationship is maintained whether  $(H - Y)\{T/D\}$  is concave up or down. Small details like this may become important in the understanding of the underlying principles of the penetrator and target shape factors and strengths as more data becomes available.

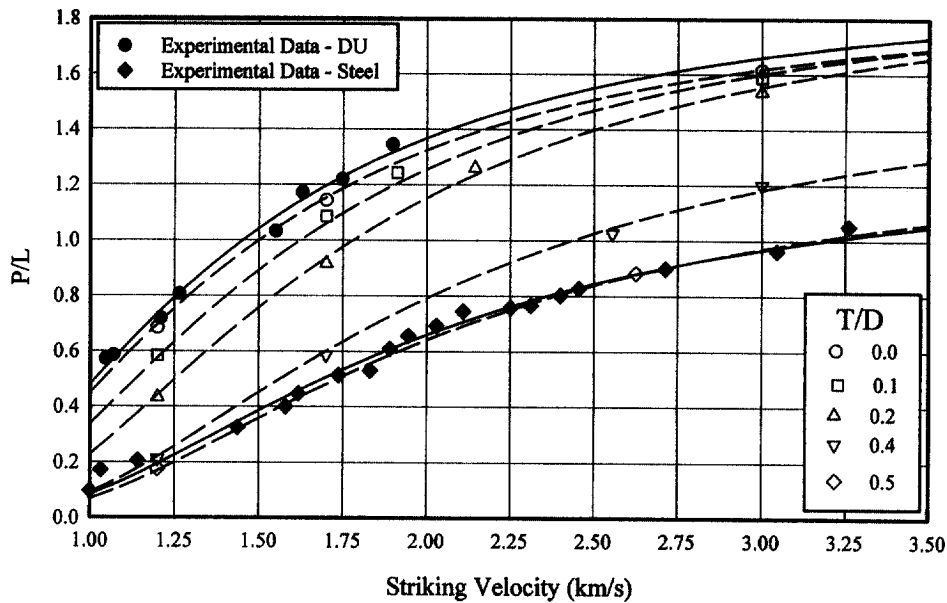


Fig. 14. Resulting curves from the “best” set of inputs to the jacketed rod penetration model.

Returning to the issue of the best input parameters, the following statements can be made after examining all of the information. First, the simulations are in agreement with the experimental data. Second, the semiempirical model described by Eqns (1) and (2) provides an exceptional fit to the experimental and simulation data. And third, regardless of the function used for  $(H - Y)\{T/D\}$ , the resulting errors between the model and the data are about the same. Although the different forms of  $(H - Y)\{T/D\}$  return similar errors, they do not return the same result, and since the results from the cases studied provide similar errors (Table 7), appearance of the resulting model, or more specifically, asymptotic lines of constant  $T/D$  become the deciding factor in determining the best set of inputs to the model. Therefore, a second-order expression for  $(H - Y)\{T/D\}$  was selected, and even though the second-order functions fitting the  $k_p$  and  $k_t$  simulation data points are physically more attractive because of their lower order, the third-order functions were selected since they fit the data better. The resulting penetration model is displayed in Fig. 14 and the functions representing  $(H - Y)\{T/D\}$ ,  $k_p$ , and  $k_t$  in Eqns (4a)–(4d).

Even though many assumptions were made and the underlying model contains only two parameters, the simulation data incorporates into the proposed model [Eqns (1), (2), and (4a)–(4d)] extremely well. The transition from DU rods to steel rods via increasing jacket thickness is smooth and agrees with intuition. Furthermore, the ability of a two-parameter fit to capture the penetration phenomena over a large velocity range is clearly supported, especially by the steel experimental data. Arguments on the appropriate shape of the  $(H - Y)\{T/D\}$ ,  $k_p$ , and  $k_t$  curves with respect to  $T/D$  can be investigated further, but as

demonstrated within this document, it is safe to say that they are not constant and represents an area for future research.

$$\alpha = 1.256, \quad (4a)$$

$$(H - Y)\left(\frac{T}{D}\right) = 10\left(\frac{T}{D}\right)^2 - 7\left(\frac{T}{D}\right) + 5.1, \quad (4b)$$

$$k_p\left(\frac{T}{D}\right) = 2.911\left(\frac{T}{D}\right)^3 - 1.865\left(\frac{T}{D}\right)^2 + 0.012\left(\frac{T}{D}\right) + 0.471, \quad (4c)$$

$$k_t\left(\frac{T}{D}\right) = 3.489\left(\frac{T}{D}\right)^3 + 0.310\left(\frac{T}{D}\right)^2 - 1.357\left(\frac{T}{D}\right) + 0.490. \quad (4d)$$

#### 4. Conclusions

A multiphase computational study was performed to examine the systemic effects of placing a jacket (sheath) on a long rod KE penetrator. Part one of the initial phase examines the penetration of finite and semi-infinite RHA targets by DU penetrators with steel sheaths. The computational results support the following two conclusions: (1) To minimize penetration degradation, the sheath must be thin,  $T/D \leq 0.1$ ; sheath thicknesses of  $T/D = 0.2$ – $0.3$  may be possible if the striking velocity is increased; (2) a thin sheath may slightly increase the residual energy of the penetrator after the target is perforated. However, as stated, these findings are based on computations only, experimental confirmation remains to verify these results due to the small differences supporting the conclusions.

In the later phases of the study, a general penetration model was developed. A two-parameter, exponential function proposed by Lanz and Odermatt was modified to include penetrator and target shape factors and penetrator and target strengths. This form fit the simulation data extremely well and also extrapolated to monolithic DU and steel experimental data. The penetration model used a bulk density assumption which was shown to be questionable and requires additional investigation once the simulation results are verified by experiments. Regardless of the assumptions, the model is simple, elegant, and quite useful to identify regions where more detailed investigations could be profitably made, and flexible enough to be adapted as new information becomes available. Finally, further computational and analytical modeling supported by experimentation of jacketed rods could provide a method for detailed observation of the important, but ill defined,  $k_p$  and  $k_t$  parameters.

#### References

- [1] Lanz W, Odermatt W. Penetration limits of conventional large caliber anti-tank guns/kinetic energy projectiles. In Proc 13th Int Symp on Ballistics, Stockholm, Sweden, 1–3 June (1992).
- [2] Burton LW, Anderson RD. Performance estimates of future projectiles utilizing advanced sabot and propulsion technologies. ARL-TR-369, U.S. Army Research Laboratory, APG, MD, March 1994.

- [3] Sorensen BR. Analysis of M1A3 KE Weapons System Performance: Solid Propellant or ETC, 120-mm or 140-mm? In Proc Third Ballistics Symp on Classified and Controlled Topics, Applied Physics Laboratory, Laurel MD, November 1995.
- [4] Ekbohm L, Holmberg L, Persson A. An armor-piercing projectile with spiculating core. In Proc 13th Int Symp on Ballistics, Stockholm, Sweden, 1–3 June 1992.
- [5] Cullis IG, Lynch NJ. Hydrocode and experimental analysis of scale size jacketed KE projectiles. In Proc 14th Int Symp on Ballistics, Quebec, Canada, 1993.
- [6] Lehr HF, Wollman E, Koerber G. Experiments with jacketed rods of high fineness ratio. *Int J Impact Engng* 1995; 17.
- [7] Sorensen BR, Zukas JA, Kimsey KD. Computational study of integrating sheathed penetrators into KE cartridges. In Proc. 19th Army Sci. Conf., Orlando FL, 20–24 June 1994.
- [8] Lanz W, Lehr HF. Craters caused by jacketed heavy metal projectiles of very high aspect ratios impacting steel targets. In Proc. 15 Int. Symp. on Ballistics, San Francisco, CA, 23–28 September 1996.
- [9] McGlaun M, Thompson SL, Elrick MG. CTH: A three-dimensional shock wave physics code. *Int J Impact Engng* 1990;10(1–4).
- [10] Nicholas T. Dynamic tensile testing of structural materials using a split-Hopkinson bar apparatus. AFWAL-TR-4053, USAF Materials Laboratory, 1980.
- [11] Bertholf LD, Buxton LD, Thorne BJ, Byers RK, Stevens AL, Thompson SL. Damage in steel plates from hypervelocity impact II. numerical results and spall measurement. *J Appl Phys* 1975;46:3776–3783.
- [12] Johnson GR, Stryk RA, Holmquist TJ, Souka OA. Recent EPIC code developments for high velocity impact: 3D element arrangements and 2D fragment distributions. *Int J Impact Engng* 1990;10(1–4).
- [13] Bjerke TW, Zukas JA, Kimsey KD. Penetration performance of disk shaped penetrators. *Int J Impact Engng* 1992;12(2).
- [14] Creighton BM. Numerical resolution calculation for elastic-plastic impact problems, BRL-MR-3418, U.S. Army Ballistic Research Laboratory, APG, MD, 1984.
- [15] Johnson GR, Cook WH. A constitutive model and data for metals subjected to large strains, high strain rates, and high temperatures. In Proc Seventh Int Symp on Ballistics, The Hague, Netherlands, April 1983.
- [16] Magness LS, Farrand TG. Deformation behavior and its relationship to the penetration performance of high density KE penetrator materials. In Proc 1990 Army Science Conference, Durham, NC, May 1990.
- [17] Anderson CE, Morris BL, Littlefield DL. Penetration Mechanics Database, Southwest Research Institute, San Antonio, TX, January 1993.
- [18] Gooch WA, Burkins MS, Frank K. Ballistic performance of titanium against laboratory penetrators. In Proc 1st Australasian Congress on Appl Mech, Melbourne, Australia, 21–23 June, 1996.
- [19] Frank K. Private communications, U.S. Army Research Laboratory, APG, MD, 1996.
- [20] Frank K. Private communications, U.S. Army Research Laboratory, APG, MD, 1993
- [21] Magness LS, Zook J. Private communications and unpublished data, U.S. Army Research Laboratory, APG, MD, 1996.